Research Article

Analysis and Evaluation of Effective Environmental Indicators in the Heat Island of District 1 of Tehran using (RS)

Ali Sayyadi, Mohammad Javad Amiri *

Faculty of Environment, College of Engineering, University of Tehran, Tehran, Iran.

P A P E R   I N F O

A B S T R A C T

One of the environmental problems today is the rising land surface temperature and the formation of heat islands in metropolitan areas, which have arisen due to the unplanned expansion of these cities. Satellite imagery is widely used in urban environmental studies to provide an integrated view and reduce costs and time. In this study, Landsat satellite imagery in TM, ETM+, and OLI sensors from 1984 to 2020, remote sensing techniques, and GIS is used to analyze the data, and SPSS software is employed to examine the correlation between the data. The results indicate that the land surface temperature in District 1 of Tehran has increased during the last 38 years. Moreover, land use in District 1 has changed significantly over this period, and urban land use increased from 16 % (1984) to 35 % (2020) while vegetation declined from 32 % to 14 %. The results of linear regression analysis show a significant correlation between satellite images and weather station data. The significance coefficient (Sig) in all stations is less than 0.05 with a 95 % confidence interval. Besides, the coefficient of variation (R) for all stations is above 80 %, and the coefficient R2 has a desirable value. The findings suggest that the trend of rising temperatures in District 1 of Tehran has become an environmental problem and the changes in land use such as declining vegetation and increasing the acceleration of urbanization are among the factors that affect it.

1. INTRODUCTION

The acceleration of urbanization in the world is increasing. To be specific, 55.3 % of the world population lived in cities in 2015. The population may increase to 68.4 % by 2050 (United Nations Department of Economic and Social Affairs, 2019). The acceleration of urbanization leads to climate change and greenhouse gas emission. Urbanization dramatically reduces vegetation and changes radiance, heat, humidity, roughness, and urban surface diffusion (Al-Hatab et al., 2018). Urbanization continuously increases artificial surfaces, including roads and buildings, changes radiative fluxes and climates, intensifies urban warming, and forms urban hotspots (Lia et al., 2020; Tepanosyan et al., 2021). The spread of this phenomenon creates an urban heat island (El-Hadidy, 2021).

Urban heat island is formed in cities or metropolises due to human-induced changes to land surfaces when urban areas experience higher temperatures than the rural ones. Natural land surfaces are replaced by urban materials such as buildings, roads, and other asphalt areas and then, heat islands come into being (Mendez-Astudillo et al., 2020; Macintyre, 2021; Kabano et al., 2021). This increase in temperature starts at 2 °C and can increase to several °C (Harun et al., 2020).

Heat island causes irreparable damage to humans and the environment. Urban heat island is a principal factor affecting urban climatology, including urban vegetation and air pollution (Li et al., 2021), environmental and human health, including vulnerable groups (Wang et al., 2021), and public health (Sekertekin & Zadbagher, 2021; Vasenev et al., 2021), include an increasing mortality rate (Koopmans et al., 2020). Therefore, the heat island must be controlled. One approach to controlling and monitoring the heat island is the combined use of RS and GIS. Many researchers have merged RS and GIS (Liu et al., 2021). RS satellites provide a simple way to investigate thermal differences between urban and rural areas, LST recovery, and urban heat islands (Ahmed, 2018). A review of the relevant lectures and records shows that the term heat island was first proposed by Howard about a century ago, in 1833. Further research indicates that urbanization has caused significant changes in the meteorological parameters and features of the earth's surface and, as a result, has given rise to many changes in the local weather and climate. Guo et al (2020) and Galdies & Lau (2020) investigated the effect of urban heat islands, extreme temperatures, and long-term climate change in Hong Kong. This study showed that despite the severe heat island effects between urban and suburban areas, urban parks could

---

*Corresponding Author's Email: mjamiri@ut.ac.ir (M.J. Amiri)
URL: https://www.jree.ir/article_163301.html

minimize the effect of heat islands. They recommend several adaptation measures related to urban spatial planning concerning climate change. Galdies & Lau (2020) and Portela et al (2020) investigated the effect of urban and industrial characteristics on the earth's surface temperature. The results showed that high LST values were concentrated in urban and industrial areas with buildings, impermeable pavements, and scattered vegetation. Urban areas with weak vegetation form intense heat islands (Portela et al., 2020). Lemus-Canovas et al. (2019) estimated the hot and cold poles of Barcelona metropolis by calculating the Earth's surface temperature from Landsat 1. The results illustrated that the heat poles were primarily concentrated in industrial and urban areas. Cold poles are found in urban green areas as well as forest areas. The maximum temperature range between land surface covers was observed in spring and summer, while this difference was insignificant in winter. This study showed that the air temperature in green areas reached up to 2.5 degrees Celsius lower than in urban areas (Lemus-Canovas, 2019). Recent studies exploring the city of Tehran demonstrate that the minimum temperatures in Tehran have increased compared to the Varamin station, which indicates the release of more thermal energy in Tehran than that in its suburbs (Akbari, 2000). Studies related to Tehran's thermal island show that the effect of Tehran's thermal island has become more apparent, and along with the growth and development of the metropolis of Tehran, the spatial and temporal characteristics of the thermal island have changed. The spatial structure of the ground surface temperature, the effects of Tehran's thermal island, and the methods of obtaining temperature in hot and polluted areas are of particular importance (Sadeghinia et al., 2013).

According to the findings of (Galdies & Lau, 2020; Guo, 2020; Portela et al., 2020), the influencing factors in the formation of heat islands include the amount of vegetation and changes in the residential context as well as the type of materials, which in this thesis has also been examined firstly by examining the changes in the residential context and the vegetation status of the area with the NDVI index. Galdies & Lau (2020) and Portela et al (2020) Both investigated the thermal island utilizing LST. In this study, LST was also used to investigate the condition of the thermal islands. In this research, in addition to examining the thermal island, an exaggerated digital elevation model map of the first region of Tehran was also prepared and Has been studied. In addition to the studies mentioned above, the correlation between the data has been investigated, and due to the relative nature of the data, Pearson and Spearman tests have been used. Another advantage of this research is the regional survey (past research is generally carried out in the country (Galdies & Lau, 2020) or carried out in the city (Portela et al., 2020)). This study aimed to investigate the state of heat islands and the factors affecting them in District 1 of Tehran using RS technology, Landsat satellite images, and thermal bands from 1984 to 2020 with emphasis on LST, land use, vegetation, and changes in height and geometry shape is done.

2. METHOD

2.1. The location of the study area

Tehran metropolis consists of 22 districts. District 1 is one of the urban areas of Tehran located at the northeastern tip and the northernmost point of Tehran, along the longitudes of 534272.5 east and 5446670.5 west and the latitudes of 3964923.5 north and 3964923.5 south. The district is limited to Alborz Mountains from the north, the Evin region from the west, Parkway and Sadr Highway from the south, and Lavasanat from the east. District 1 of Tehran is a part of Shemiranat city. The district is also known as Shemiran. According to the 2016 census of Iran, the population of this district is 487,508 people (166,881 households) and an area of about 8944/3604 hectares. The location of District 1 and the divisions of the districts are shown in Figure 1.
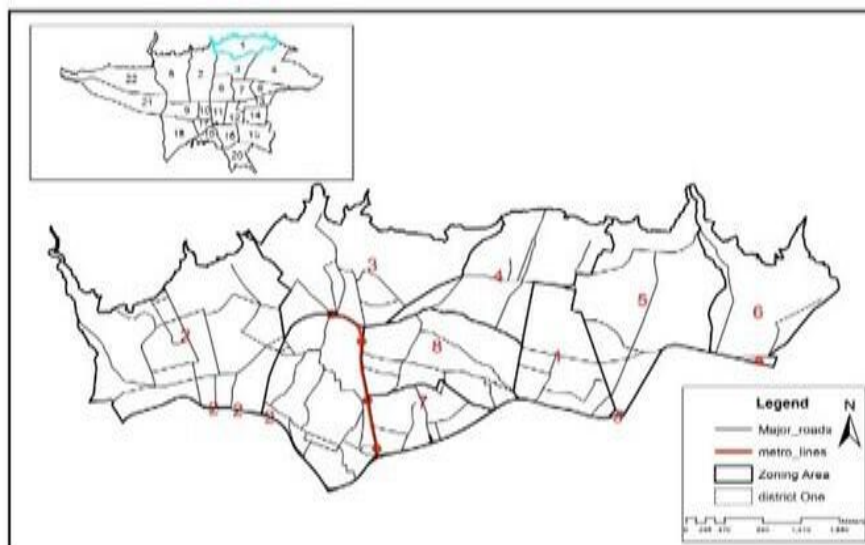

Figure 1. Location of study area

2.2. Methodology

This is a descriptive-analytical and applied study in terms of purpose. This study uses Landsat satellite images for environmental and spatial analyses of District 1. To this end, Landsat satellite images in TM-ETM-OLI sensors for the years 1984, 1994, 2004, 2014, and 2020 are available on the United States Geological Survey (USGS) website and NASA. This study uses thermal RS techniques (including 10 Landsat satellite images) and GIS that have been effectively and efficiently combined to investigate the factors affecting LST and the formation of a heat island in District 1 due to its special

topographic conditions. One of the most important factors is the increase in LST, which, as mentioned, is measured using thermal RS in the summer and winter. Another factor is the study of vegetation in the study area from 1984 to 2020 using the Normalized Difference Vegetation Index (NDVI) and the three-dimensional shape and elevation of the area. Another factor is land use, which refers to the characteristics of homogeneous and repetitive components and features of the land surface, which can be distinguished from other features with a clear boundary. The basis of the land study is the land

cover map information that must be extracted from raw RS data and then classified before entering the GIS. The classification of satellite images is the most crucial part of satellite data interpretation. In this study, the images prepared from 1984 to 2020 are analyzed and classified to examine changes in land use in District 1. RS data collected from the land surface by various sensors may be subject to shortcomings and errors. Thus, deficiencies must be compensated and errors eliminated using satellite imagery. ARC GIS 10.8, Envi5.2, and SPSS are used to output, process, and analyze Landsat images.

Table 1. Landsat satellite imagery specifications

Date of taking the image	Satellite	Sensor	PATH	ROW	Thermal band
1984-04-25	LANDSAT_5"	"TM"	164	035	6
1984-11-19	LANDSAT_5"	"TM"	164	035	6
1987-07-07	LANDSAT_5"	"TM"	164	035	6
1987-01-12	LANDSAT_5"	"TM"	164	035	6
1990-07-31	LANDSAT_5"	"TM"	164	035	6
1990-12-22	LANDSAT_5"	"TM"	164	035	6
1992-01-26	LANDSAT_5"	"TM"	164	035	6
1992-08-05	LANDSAT_5"	"TM"	164	035	6
1994-01-15	LANDSAT_5"	"TM"	164	035	6
1994-08-27	LANDSAT_5"	"TM"	164	035	6
1996-08-23	LANDSAT_5"	"TM"	164	035	6
1996-10-10	LANDSAT_5"	"TM"	164	035	6
1998-01-26	LANDSAT_5"	"TM"	164	035	6
1998-08-06	LANDSAT_5"	"TM"	164	035	6
2000-01-16	"LANDSAT_7"	"ETM"	164	035	6
2000-08-11	"LANDSAT_7"	"ETM"	164	035	6
2002-01-13	"LANDSAT_7"	"ETM"	164	035	6
2002-08-09	"LANDSAT_7"	"ETM"	164	035	6
2004-01-19	"LANDSAT_7"	"ETM"	164	035	6
2004-08-14	"LANDSAT_7"	"ETM"	164	035	6
2006-02-25	"LANDSAT_7"	"ETM"	164	035	6
2006-08-04	"LANDSAT_7"	"ETM"	164	035	6
2008-01-14	"LANDSAT_7"	"ETM"	164	035	6
2008-08-09	"LANDSAT_7"	"ETM"	164	035	6
2010-01-03	"LANDSAT_7"	"ETM"	164	035	6
2010-08-15	"LANDSAT_7"	"ETM"	164	035	6
2012-01-25	"LANDSAT_7"	"ETM"	164	035	6
2012-08-04	"LANDSAT_7"	"ETM"	164	035	6
2014-01-14	"LANDSAT_7"	"ETM"	164	035	6
2014-08-10	"LANDSAT_7"	"ETM"	164	035	6
2016-02-03	"LANDSAT_8"	"OLI_TIRS"	164	035	10-11
2016-08-15	"LANDSAT_8"	"OLI_TIRS"	164	035	10-11
2018-01-25	"LANDSAT_8"	"OLI_TIRS"	164	035	10-11
2018-08-05	"LANDSAT_8"	"OLI_TIRS"	164	035	10-11
2020-01-15	"LANDSAT_8"	"OLI_TIRS"	164	035	10-11
2020-08-10	"LANDSAT_8"	"OLI_TIRS"	164	035	10-11

2.3. Land use

One of the factors affecting the increase in temperature in District 1 is land use because this district, like other districts of Tehran, has experienced its fair share of spatial changes in different years, which have significantly increased the city's temperature at different times. Remote sensing, which aims to identify and separate land phenomena and classify them, and Landsat satellite imagery from 1984 to 2020 were used to study these changes. Band composition in Landsat images is one of

the methods used to obtain a land-use map before classification. This study uses the 2-3-4 band combination for TM, ETM+, and OLI sensors. In this combination, band 4 is the infrared band, with the vegetation having the highest reflectance. Band compositions for preparing land-use maps for District 1 of Tehran from 1984 to 2020 can be seen in Figure 2. As seen in the figure, the study area is divided into five classes: green space and vegetation in green, urban land use in pink, barren and abandoned lands in white, poor lands or mountains in purple, and roads in black.
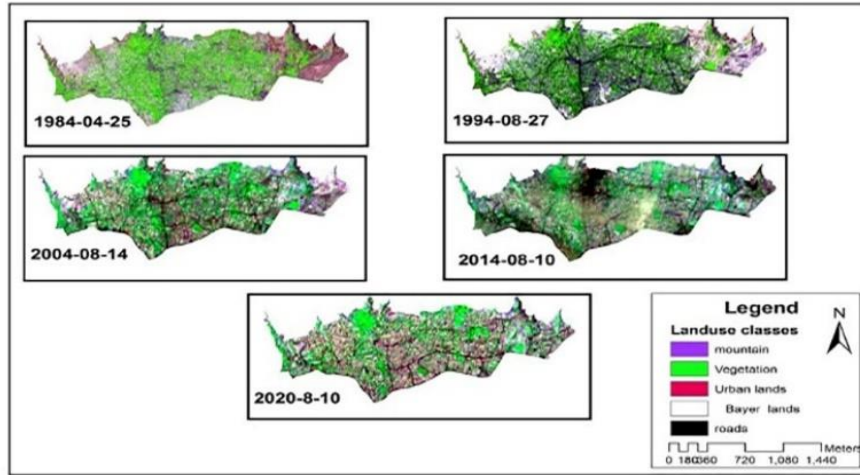
Figure 2. Land-use map

After color composition, also called visual interpretation, digital processing is used to classify the images of the study area so that some areas are first selected as a sample or class, and the classification is performed using the maximum likelihood estimation, which has been mentioned as the most accurate and widely used method of classifying images. After classification, its accuracy, considered a criterion for classification valuation, is checked. The overall accuracy of the classification is calculated using Equation (1) as follows (Makhdoom et al., 2004):

$$\text{Overall accuracy} = \frac{\text{The sum of the pixels that are correctly classified}}{\text{The whole pixels of the image}} \ldots (1)$$

The generated accuracy is a measure of the correct classification of the pixels of a class relative to the same class in the ground truth. It is expressed in Equation (2) (Makhdoom et al., 2004):

$$\text{the accuracy of the producer of class x} = \frac{\text{Total correctly classified pixels of class X}}{\text{The desired pixels in the ground truth}} \quad (2)$$

Besides, user accuracy indicates the probability that a pixel in a classified map belongs to the same class. User accuracy, which is the knowledge of the degree of confidence in the generated map, is calculated via Equation (3) as follows (Makhdoom et al., 2004):

$$\text{Class x user accuracy} = \frac{\text{Total correctly classified pixels of class X}}{\text{Class x pixels on the map}} \quad (3)$$

Finally, the k coefficient, which represents the agreement between the classification and the ground truth data, has a range between 0 and 1, in which 1 indicates the complete agreement between the classified map and the ground truth data (Makhdoom et al., 2004). The k coefficient is calculated via Equation (4):

$$k = \frac{\theta_2 - \theta_1}{\theta_2 - 1} \quad (4)$$

where θ1 is the overall accuracy and θ2 is the contingent agreement, which is calculated as follows (Makhdoom et al., 2004):

$$\theta_2 = \text{Ⅱ} \quad Xi + \text{Ⅱ} \quad x + \frac{i}{N} \quad (5)$$

There are several models and methods for classification using RS. This study uses the maximum likelihood estimation due to its high classification accuracy and reliability.

2.4. Land Surface Temperature (LST)

One of the most critical factors affecting the increase in temperature of District 1 is LST, which is obtained by the thermal bands of Landsat satellites in TM, ETM+, and OLI sensors. The pixels of the images must first be processed to obtain correct information to prepare a thermal map of the city. All of these are called image pre-processing or image correction. One of the most critical corrections applied to image pixels is radiometric. One part of radiometric corrections of images is spectral correction performed on Digital Numbers (DNs) or the pixel so that when the image is taken, it has DNs. These DNs contain information about land surface phenomena. However, the initial data contains basic information (uncorrected) and cannot represent the land surface parameters such as temperature, humidity, vegetation, etc. The DNs of the satellite imagery must be corrected to apply the values of the ground surface parameters to the desired satellite imagery. The DNs of each image must be converted into radiance and reflectance. This form of correction is referred to as spectral correction. Several models and methods for converting the DNS of satellite images into radiance and reflectance are referred to below. Equation (6) converts raw image values into radiance for Landsat TM and ETM images (Chander et al., 2009).

$$L\lambda = \left(\frac{\text{LMAX} - \text{LMIN}}{\text{Qcalmax} - \text{Qcalmin}}\right)(\text{Qcal} - \text{Qcalmin}) + \text{LMIN} \quad (6)$$

where Lλ is the spectral radiance in the sensor, Qcal is the pixel value (DN) in the desired band, Qcalmin is the minimum pixel value (DN), Qcalmax is the maximum pixel value (DN), and LMIN and LMAX are minimum and maximum spectral radiances in the sensor. This file is available and can be downloaded in the metadata file of every satellite image. Moreover, the reflectance coefficient for the Landsat TM5.ETM7 sensor is calculated based on Equation (7) (Chander et al., 2009):

$$p\lambda = \frac{\pi \times L\lambda \times d^2}{\text{ESUN } \lambda \times COS\ \theta S}) \quad (7)$$

where pλ is the reflectance coefficient, π = 3.1459, Lλ is the spectral radiance in the sensor, d is the distance between the

earth and the sun (astronomical unit), ESUN is the average of the sun's rays, and θ is the angle of the sun's rays (degrees).

Equation (8) is used to obtain the spectral radiance in the OLI sensor (Chander et al., 2009):

$$L\lambda = ML * Qcal + AL \qquad (8)$$

where Lλ is the radiance above the atmosphere (watts/m^2*srad*μm), ML is the multiplicative conversion factor, Qcal is the pixel values (DNs) 10 and 11, and AL is the aggregate conversion factor.

2.5. Obtain the brightness temperature

Thermal band data can be converted from spectral radiance in the sensor into brightness temperature, assuming that the earth is a black body and includes the effects of the atmosphere (absorption and radiance). The brightness temperature for Landsat satellite sensors is calculated from Equation (9) (Rajeshwari & Mani, 2014).

$$T = \frac{K2}{Ln(\frac{K1}{L\lambda}+1)} \qquad (9)$$

where T is the temperature affecting the brightness in the sensor in Kelvin; L is the spectral radiance of the meter in terms of (Wm^{-2}sr^{-1}um^{-1}). The values of K1 and K2 are the first and second calibration constants (Wm^{-2}), respectively, and the coefficients of K1 and K2 are calculated in Table (2).

Table 2. Coefficients K1 and K2 for Landsat satellite

Sensor coefficient (band)	Calibration coefficient (K1)	Calibration coefficient (K2)
L5-TM B6	607.76	1260.56
L7-ETM+B6	666.09	1282.71
L8-OLI B10	777.89	1321.08
L8-OLI B11	480.89	1201.14

2.6. Vegetation

One of the other factors affecting the temperature increase in District 1 is its vegetation density, which is obtained using Landsat satellite images and NDVI. NDVI is calculated based on Equation (10) (VAN de Griend & Owe,1993):

$$NDVI = \frac{NIR-RED}{NIR+RED} \qquad (10)$$

where NIR is the reflectance in the infrared band, and RED is the reflectance in the red band. Although the value of this index is in the range of -1 and 1 theoretically, in practice, it is less than (1) and more than -1. The values of this index for dense vegetation tend to be 1, but negative values characterize clouds, snow, and water, and rocks and barren soils with similar spectral reactions used in the two bands are seen with values close to zero. In this index, typical soil is considered equal to 1. The higher the pixel distance from the soil size, the denser the vegetation. In this regard, NDVI is applied to Landsat images. The vegetation map of District 1 of Tehran has been complied and prepared from 1984 to 2020 in five classes: very light red, relatively light orange, medium-density yellow, relatively high light green, and very high-density dark green.

2.7. Changes in elevation

Another factor affecting climate, environmental, and thermal changes in District 1 is the changes in elevation and geometric and three-dimensional shape of this district so that most of the areas and neighborhoods of the district are located at high altitudes (for example, Punak, Islamic Azad University, Science and Research Branch, Hesarak, etc.). As shown in Figure 3 (digital elevation model map of District 1 with an accuracy of 5 m), most areas and neighborhoods of this district are located at altitudes between 1400 and 1835.

Figure 3. Digital elevation model map
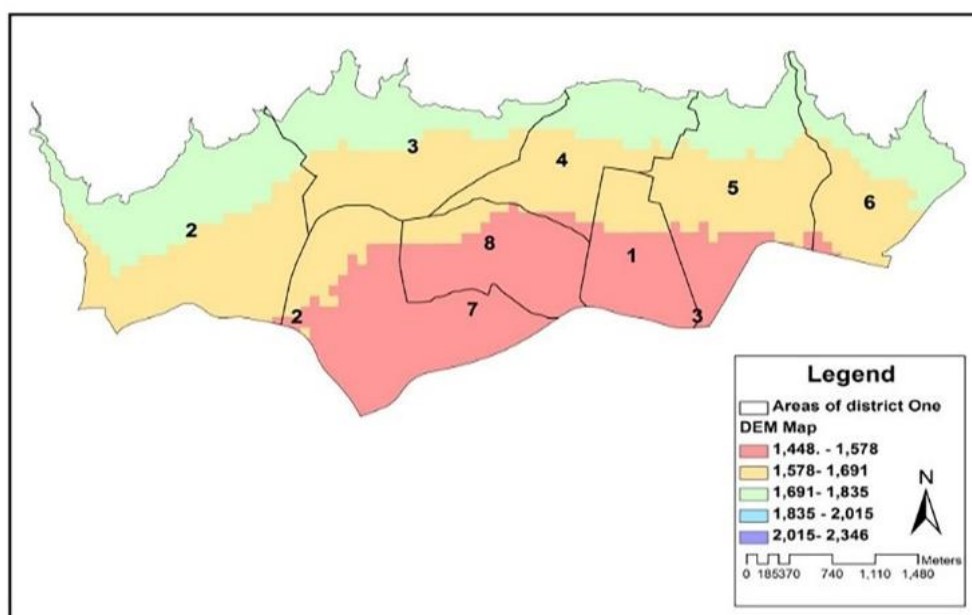
Figure (4) is slightly exaggerated and shows the mountains, poor terrain, and high altitudes of most of the neighborhoods and residential areas of District 1 of Tehran. These areas are located like a hole around these mountains. Like a barrier, these mountains and poor terrain prevent winds and cyclones from entering the district and, consequently, increase the temperature in the district.
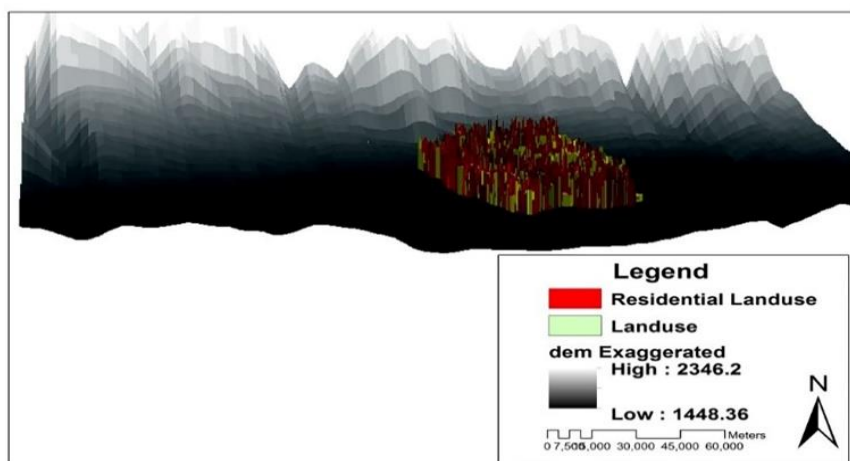
Figure 4. Exaggerated map of digital elevation model

2.8. The correlation between LST and weather stations

Data in the studied years were received from reputable centers (Table 3), and the correlation between the surface temperature of stations and Landsat images was obtained using SPSS software and the linear regression method to examine the correlation between satellite images and weather stations.

Table 3. Weather stations in Tehran

Year	Tehran station	Shemiran station	Chitgar station	Geophysics station
1984-04-25	17.7	13.7	15.4	3.5
1984-11-19	11.4	9.4	11.6	12.3
1994-08-27	31.2	28.9	33.1	31.5
1994-01-15	-6	4.1	6.7	5.7
2004-08-14	31.4	27.9	31.9	31.1
2014-01-14	5.3	3.7	7.3	5.5
2020-08-20	36.9	36.5	38.3	35.6
2020-01-15	8.2	7.6	9.2	6.6

The linear regression model assumes a linear relationship (or a straight line) between the dependent variable and each predictor, as described in Equation (11).

$$y_i = b_0 + b_1 x_{i1} + ... + b_p x_{ip} + e_i \qquad (11)$$

where:
y_i is the value of item i of the quantitative dependent variable.
p is the number of predictors.
b_j is the value of coefficient j, $j = 0, ..., p$
X_{ij} is the value of item i of predictor j.

e_i is the error in the observed value for item i.

The model is linear because increasing the predictor j by 1 unit increases the dependent value of the units b_i. It should be noted that b_0 is the intercept. b_0 will be the value of the dependent variable predictor model when the value of each predictor is zero. The initial condition for linear regression is the normal distribution of data. Therefore, the normal distribution of data is first checked using the Smirnov test (Tables 4 and 5).

Table 4. Smirnov test to check the normal distribution of data for satellite images

One-sample Kolmogorov-Smirnov test		Blue class	Green class	Yellow class	Orange class
N		10	10	10	10
Normal parameters [a,b]	**Mean**	4.050	8.250	12.850	1486080.0000
	Std. deviation	19.0299	19.1184	20.3880	1840520.55245
Most extreme differences	**Absolute**	.173	.164	.182	.186
	Positive	.173	.164	.167	.140
	Negative	-.171	-.155	-.182	-.186
Test statistic		.173	.164	.182	.186
Asymp. Sig. (2-tailed) test distribution is normal.		.200 [c,d]	.200 [c,d]	.200 [c,d]	.200 [c,d]

a: Test distribution is normal.
b: Calculated from data.
c: Liliefors Significance Correction.
d: This is a lower bound of the true significance.

Table 5. Smirnov test to check the normality of data distribution for weather stations

One-sample Kolmogorov-Smirnov test		Tehran station	Shemiran station	Chitgar station	Geophysics station
N		10	10	10	10
Normal parameters [a,b]	**Mean**	17.40	16.49	19.18	16.73
	Std. deviation	14.535	12.688	13.124	13.429
Most extreme differences	**Absolute**	.229	.216	.234	.275
	Positive	.160	.212	.218	.275
	Negative	-.229	-.216	-.234	-.237
Test statistic		.229	.216	.234	.275
Asymp. Sig. (2-tailed) test distribution is normal.		.147[c]	.200[c,d]	.129[c]	.031[c]
a: Test distribution is normal.					
b: Calculated from data.					
c: Liliefors Significance Correction.					
d: This is a lower bound of the true significance.					

According to the above tables, the data are distributed normally. The correlation between the data is then examined. Pearson and Spearman's tests are used because the data are relative (Tables 6 and 7).

Table 6. Pearson test for satellite images and weather stations

Pearson correlation		Blue class	Green class	Yellow class	Orange class	Red class	Tehran station	Shemiran station	Chitgar station	Geophysics station
Blue class		1	.990**	.983**	.968**	.958**	.832**	.871**	.885**	.787**
	Sig. (2-tailed)		.000	.000	.000	.000	.003	.001	.001	.007
	N	10	10	10	10	10	10	10	10	10
Green class	Pearson correlation	.990**	1	.994**	.986**	.976**	.852**	.881**	.896**	.815**
	Sig. (2-tailed)	.000		.000	.000	.000	.002	.001	.000	.004
	N	10	10	10	10	10	10	10	10	10
Yellow class	Pearson correlation	.983**	.994**	1	.997**	.985**	.846**	.856**	.870**	.766**
	Sig. (2-tailed)	.000	.000		.000	.000	.002	.002	.001	.010
	N	10	10	10	10	10	10	10	10	10
Orange class	Pearson correlation	.968**	.986**	.997**	1	.989**	.846**	.845**	.857**	.751*
	Sig. (2-tailed)	.000	.000	.000		.000	.002	.002	.002	.012
	N	10	10	10	10	10	10	10	10	10
Red class	Pearson correlation	.958**	.976**	.985**	.989**	1	.877**	.876**	.886**	.779**
	Sig. (2-tailed)	.000	.000	.000	.000		.001	.001	.001	.008
	N	10	10	10	10	10	10	10	10	10
Tehran station	Pearson correlation	.832**	.852**	.846**	.846**	.877**	1	.965**	.962**	.906**
	Sig. (2-tailed)	.003	.002	.002	.002	.001		.000	.000	.000
	N	10	10	10	10	10	10	10	10	10
Shemiran station	Pearson correlation	.871**	.881**	.856**	.845**	.876**	.965**	1	.997**	.956**
	Sig. (2-tailed)	.001	.001	.002	.002	.001	.000		.000	.000
	N	10	10	10	10	10	10	10	10	10
Chitgar station	Pearson correlation	.885**	.896**	.870**	.857**	.886**	.962**	.997**	1	.965**
	Sig. (2-tailed)	.001	.000	.001	.002	.001	.000	.000		.000
	N	10	10	10	10	10	10	10	10	10
Geophysics station	Pearson correlation	.787**	.815**	.766**	.751*	.779**	.906**	.956**	.965**	1
	Sig. (2-tailed)	.007	.004	.010	.012	.008	.000	.000	.000	
	N	10	10	10	10	10	10	10	10	10
*. Correlation is significant at a level of 0.05 (2-tailed). / **. Correlation is significant at a level of 0.01 (2-tailed).										

Table 7. Spearman test for satellite images and weather stations

Spearman's rho correlations			Blue class	Green class	Yellow class	Orange class	Red class	Tehran station	Shemiran station	Chitgar station	Geophysics station
Spearman's rho	Blue class	Correlation coefficient	1.000	.982**	.976**	.960**	.973**	.693*	.689*	.796**	.565
		Sig. (2-tailed)	.	.000	.000	.000	.000	.026	.028	.006	.089
		N	10	10	10	10	10	10	10	10	10
	Green class	Correlation coefficient	.982**	1.000	.994**	.988**	.997**	.705*	.686*	.772**	.571
		Sig. (2-tailed)	.000	.	.000	.000	.000	.023	.029	.009	.084
		N	10	10	10	10	10	10	10	10	10
	Yellow class	Correlation coefficient	.976**	.994**	1.000	.997**	.997**	.705*	.677*	.772**	.541
		Sig. (2-tailed)	.000	.000	.	.000	.000	.023	.032	.009	.106
		N	10	10	10	10	10	10	10	10	10
	Orange class	Correlation coefficient	.960**	.988**	.997**	1.000	.994**	.720*	.679*	.768**	.537
		Sig. (2-tailed)	.000	.000	.000	.	.000	.019	.031	.009	.110
		N	10	10	10	10	10	10	10	10	10
	Red class	Correlation coefficient	.973**	.997**	.997**	.994**	1.000	.721*	.693*	.782**	.576
		Sig. (2-tailed)	.000	.000	.000	.000	.	.019	.026	.008	.082
		N	10	10	10	10	10	10	10	10	10
	Tehran station	Correlation coefficient	.693*	.705*	.705*	.720*	.721*	1.000	.967**	.927**	.733*
		Sig. (2-tailed)	.026	.023	.023	.019	.019	.	.000	.000	.016
		N	10	10	10	10	10	10	10	10	10
	Shemiran station	Correlation coefficient	.689*	.686*	.677*	.679*	.693*	.967**	1.000	.948**	.778**
		Sig. (2-tailed)	.028	.029	.032	.031	.026	.000	.	.000	.008
		N	10	10	10	10	10	10	10	10	10
	Chitgar station	Correlation coefficient	.796**	.772**	.772**	.768**	.782**	.927**	.948**	1.000	.770**
		Sig. (2-tailed)	.006	.009	.009	.009	.008	.000	.000	.	.009
		N	10	10	10	10	10	10	10	10	10
	Geophysics station	Correlation coefficient	.565	.571	.541	.537	.576	.733*	.778**	.770**	1.000
		Sig. (2-tailed)	.089	.084	.106	.110	.082	.016	.008	.009	.
		N	10	10	10	10	10	10	10	10	10
*. Correlation is significant at a level of 0.05 (2-tailed).											
**. Correlation is significant at a level of 0.01 (2-tailed).											

Since the significant coefficients of the Pearson and Spearman models are less than the confidence level of 0.05, it can be argued that there is a significant relationship between the data of weather stations in Tehran and Landsat satellite images. Thus, the linear regression model can be used between them, as described in Equation (11).

3. RESULTS AND DISCUSSION

One of the most critical factors affecting the increase in temperature in District 1 of Tehran is LST. This study prepared a thermal zoning map using Landsat thermal images in ETM and TM sensors in Band (6) and Oli sensors in Bands (10) and (11) in the winter and summer from 1984 to 2020 (Figure 5). The study area was then classified into five classes: blue, green, yellow, orange, and red, each class containing the corresponding temperature in degrees Celsius (Table 8). According to Figure 5 and Table 8, the trend of temperature is ascending in District 1 in both summer and winter, indicating climate change, rising LST in District 1, and the formation of a heat island in the district.
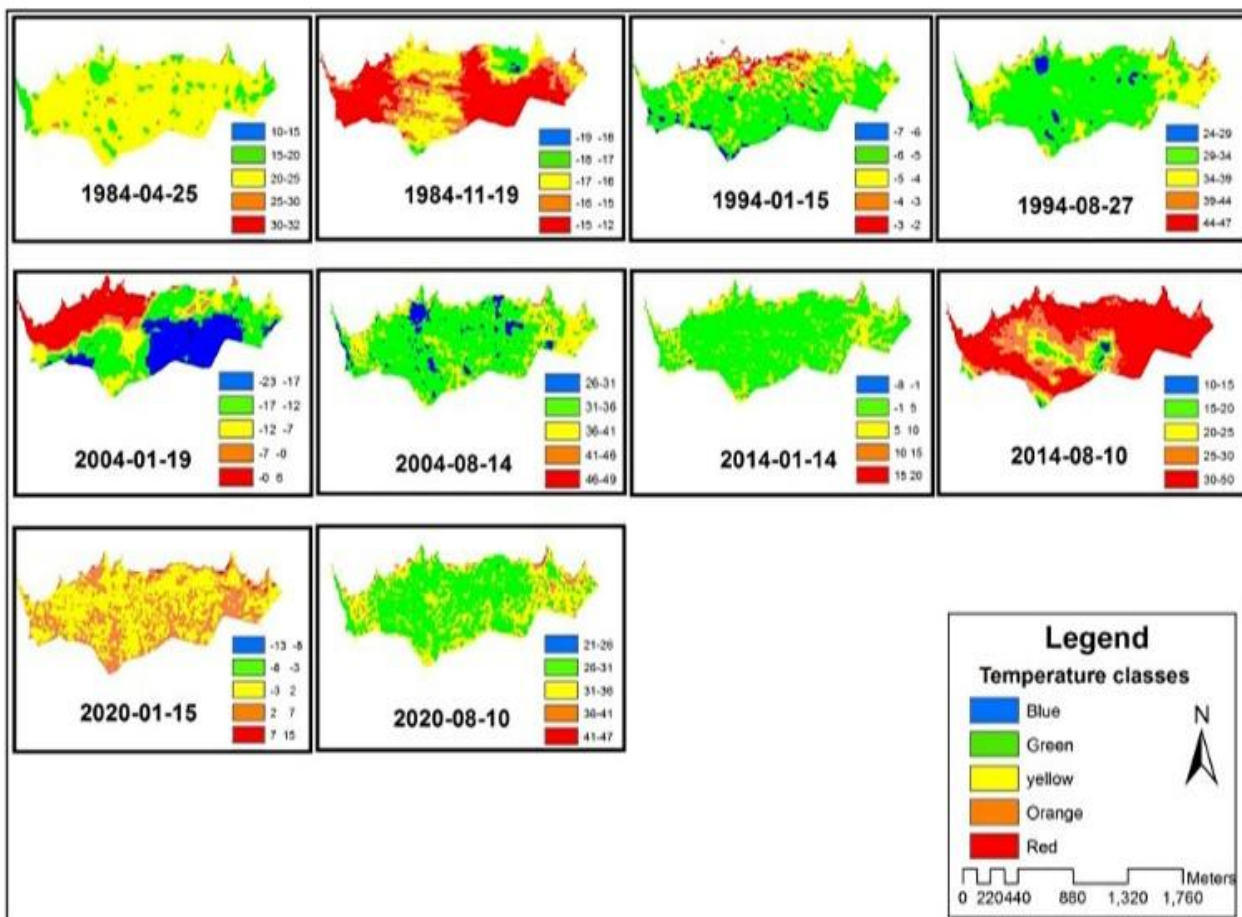
Figure 5. LST map

Table 8. LST classification using Landsat thermal images

Year	Classes				
	Blue	**Green**	**Yellow**	**Orange**	**Red**
1984_04_25	10_15	15_20	20_25	25_30	30_35
1984_11_19	-18_-19	-17_-18	-16_-17	-15_-16	-15_-12
1994_08_27	24_29	29_34	34_39	39_44	44_47
1994_01_15	-6_-7	-6_-5	-5_-4	-4_-3	-3_-2
2004_08_14	26_31	31_36	36_41	41_46	46_49
2004_01_19	-23_-17	-17_-12	-12_-7	-7_0	0_6
2014_08_10	10_15	15_20	20_25	25_30	30_50
2014_01_14	-8_-1	-1_5	5_10	10_15	15_20
2020_08_10	21_26	26_31	31_36	36_41	41_47
2020_01_15	-13_-8	-8_-3	-3_2	2_7	7-15

According to Table 8, the trend of temperature increases in District 1 has been increasing in both summer and winter; thus, the blue class in the summer (1984) was between 10 and 15 °C and changed to 21 to 26 °C in 2020. Moreover, the red class with the highest density had a temperature between 30 and 32 °C in 1984, which reached 50 °C in 2014 and 47 °C in 2020. It rose from -18 °C in winter to 15 °C in 2020.

Land use is another factor that affects LST changes in District 1 of Tehran. Land-use change map of District 1 of Tehran was prepared using Landsat satellite imagery, supervised classification, and maximum likelihood estimation from 1984 to 2020 in five classes: vegetation, urban land use, barren lands, poor lands, and mountains and roads (Figure 6).

Following the preparation of the land-use change map, the area percentage for each land-use class and the accuracy of classes with ground truth data (k) were obtained (Table 9).
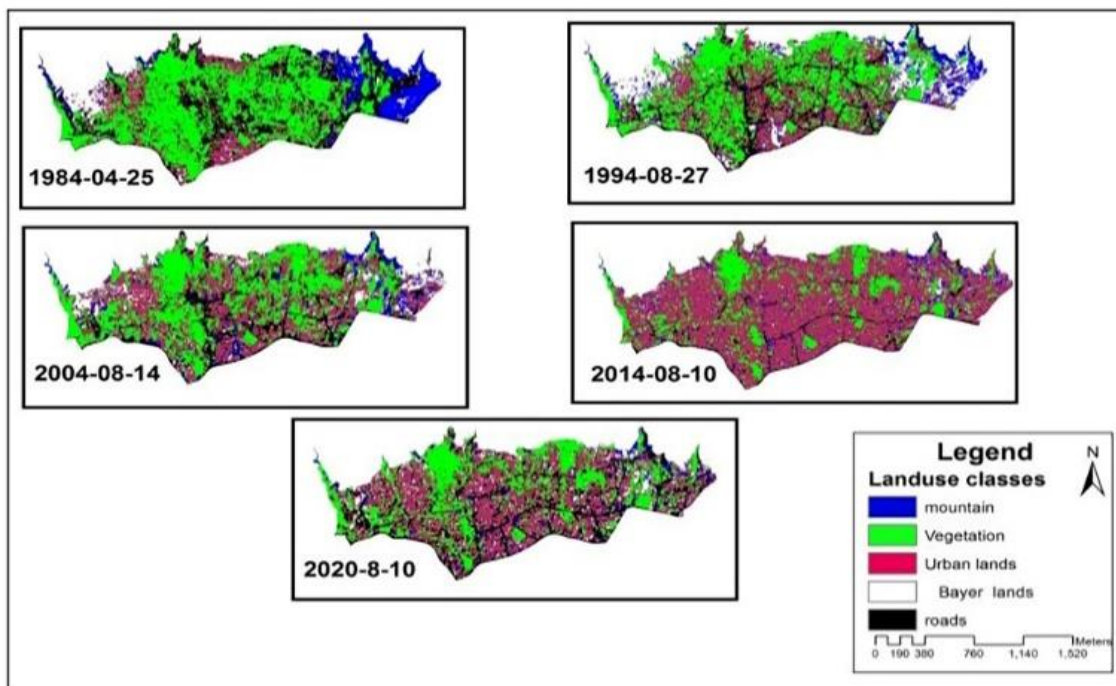
Figure 6. Land-use classification map

Table 9. The percentage of the area of each land-use class using Landsat images

Year	Land use area (%)					k coefficient (%)
	Vegetation	**Urban**	**Barren lands**	**Mountains**	**Roads**	
1984	32.597	16.795	24.039	18.594	7.976	96
1994	26.502	26.038	15.978	18.628	12.855	97
2004	26.015	32.834	11.679	15.754	13.718	97
2014	14.155	35.745	12.497	19.271	18.331	97
2020	22.065	35.949	9.909	12.820	19.257	97

According to Figure 6 and Table 9, vegetation cover was reduced from 32 % in 1984 to 26.5, 26, and 14 in 1994, 2004, and 2014, respectively, which recorded a downward trend, but increased to 22 % in 2020. Simply put, the overall trend from 1984 to 2020 was descending. Residential areas occupied 16 % of the city in 1984. After this time period, the mentioned trend took an ascending direction and reached 35 % in 2020. Moreover, barren lands decreased from 24 % to 9.9 %. According to the results of Figure 6 and Table 9, the number of mountains decreased from 18 % to 12 % and on the contrary,

the number of paths in Region 1 increased from 7.9 % to 19 %.

The land use in the case study changed significantly from 1984 to 2020 and the urban field grew from 16 % in 1984 to 35 % in 2020 while vegetation cover was attenuated from 32 % in 1984 to 22 % in 2020. Barren lands decreased from 24 % in 1984 to 9 % and roads increased sharply from 7 % to 19 % in 2020. The trend of land use in our case study from the year 1984 to 2020 is accessible in Figure 7.
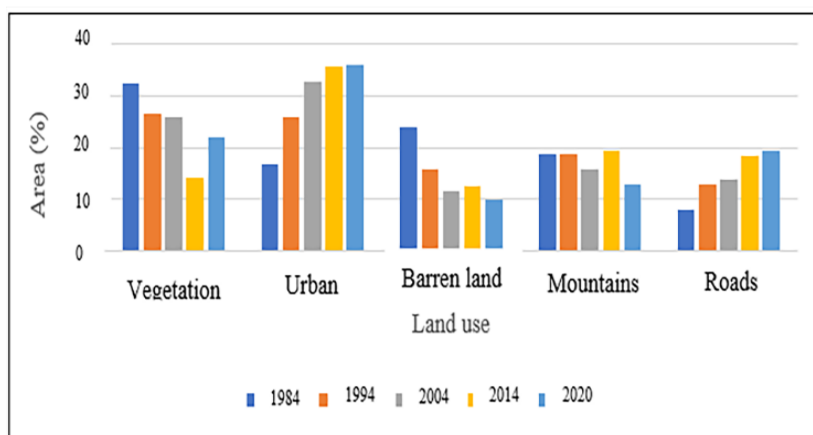

Figure 7. The trend of land-use change

Vegetation cover trends in District 1 was investigated using NDVI. This index was prepared for Landsat images in 1984, 1994, 2004, 2014, and 2020. In this map, the red dots indicate the areas devoid of vegetation, while the green dots indicate those with vegetation. However, the comparison of NDVI maps indicates the declining trend for vegetation cover over the past 38 years (Figure 8).

The results of the fitted linear regression model between weather station data and satellite images showed a significant correlation between them; therefore, the significance coefficient (Sig) of all stations was less than the confidence level of 0.05. The coefficient of variation (R) for all the stations had the desired value above 0.80. The regression analysis results indicate that the red and green classes had the highest correlation among other LST classes of satellite images (Table 10).
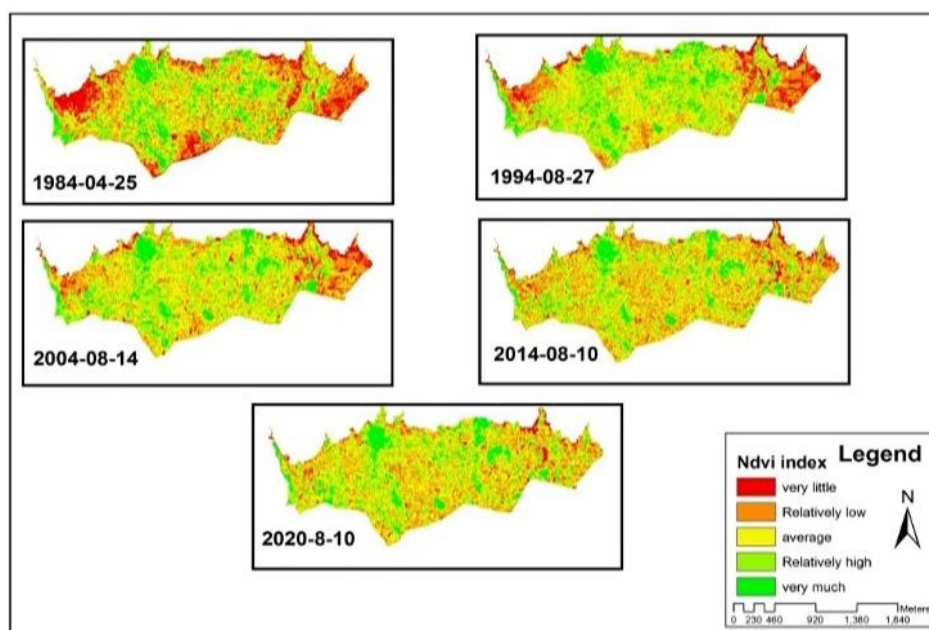

Figure 8. NDVI map

Table 10. Linear regression between satellite images and weather stations

Weather station	Class correlation	R	R²	Durbin–Watson statistic	Sig	Regression model	Standardized beta coefficient	Non-standardized beta coefficient	The predicted SD
Tehran	Red	0.877	0.769	2.618	0.001	Forward	0.877	0.553	7.410
Shemiran	Green	0.881	0.776	2.988	0.001	Forward	0.881	0.584	6.374
Chitgar	Green	0.896	0.803	2.948	0.000	Forward	0.896	0.615	6.174
Geophysics	Green	0.815	0.664	2.185	0.004	Forward	0.815	0.572	8.261
	Yellow	0.904	0.817	2.185	0.003	Forward	0.904	0.623	6.507

4. CONCLUSIONS

According to the referenced findings (Galdies & Lau, 2020; Guo et al., 2020; Portela et al., 2020), the influencing factors in the formation of heat islands include the extent of vegetation cover, changes to the residential context, and the type of materials. The current study managed to investigate the changes to the residential context and the vegetation status of the area based on NDVI index. Galdies & Lau (2020) and Portela et al (2020) both investigated the thermal island utilizing LST. In this study, LST was also used to investigate the condition of thermal islands. In the present research, in addition to examining the thermal island, an exaggerated digital elevation model map of District 1 of Tehran was prepared and studied. In addition to the studies mentioned above, the correlation between the data was investigated, and due to the relative nature of the data, Pearson and Spearman tests were employed. This research made use of the regional survey to its advantage (past research is generally carried out in the country (Galdies & Lau, 2020) or carried out in the city (Portela et al., 2020). This study aimed to investigate the state of heat islands and the factors affecting them in District 1 of Tehran using RS technology, Landsat satellite images, and thermal bands from 1984 to 2020 with emphasis on LST, land use, vegetation, and changes in height and geometry shape is done. This research is seen as necessary for future planning.

The results indicate that the trend of temperature increased in District 1 from the year 1984 to 2020 in both summer and winter. Thus, the blue class in the summer of 1984 ranged between 10 and 15 °C and changed to 21 to 26 °C in 2020. Moreover, the red class with the highest density had a temperature between 30 and 32 °C in 1984, which reached 50 °C in 2014 and 47 °C in 2020. Land use in District 1 changed significantly over this period, with urban land use increasing

from 16 % (in 1984) to 35 % (in 2020) and vegetation declining from 32 % to 14 %. Vegetation analysis using NDVI showed a decreasing vegetation trend in the studied years. A significant correlation was seen between satellite images and the data collected from weather stations such as Tehran, Shemiran, Chitgar, and Geophysics stations to validate the study using the fitted linear regression model. The results of linear regression analysis demonstrated a significant correlation between satellite images and weather station data; therefore, the significance coefficient (Sig) in the case of all the stations was less than 0.05 with a 95 % confidence interval. Besides, the coefficient of variation (R) for all the stations was above 80 %. The regression analysis results show that the red and green classes had the highest correlation among other LST classes of satellite images. Another factor affecting temperature changes in District 1 of Tehran included the elevation and geometric and three-dimensional shape of this district such that most of the areas and neighborhoods of the district were located at high altitudes between 1400 and 1835. These high altitudes hinder the positive course of natural rainfall and other climatic factors which, in turn, increase the district's temperature compared to other districts over time. The findings illustrate that rising temperatures in District 1 of Tehran show no signs of putting on the brake any time soon. Unfortunately, land-use changes such as declining vegetation and increasing urban land use exacerbate this trend. In addition, population growth and the declining vegetation cover and rising number of buildings lead to the overheating of impermeable surfaces and excess heat penetrating the environment. Population growth and land-use change cause much vegetation to disappear, only to be replaced by buildings, roads, and other urban facilities. Reducing vegetation and turning it into high-rise buildings increase the temperature of the city. It must be emphasized that vegetation is one of the main factors in respiration, absorption of urban pollutants, and good biodiversity and prevents the rise of temperature in cities. In the end, we recommend further investigation into the effect of humidity on the thermal islands of the region as well as the type of materials and their relationship with these islands.

5. ACKNOWLEDGEMENT

REFERENCES

1. Ahmed, S. (2018). Assessment of urban heat islands and impact of climate change on socioeconomic over Suez Governorate using remote sensing and GIS techniques. *The Egyptian Journal of Remote Sensing and Space Sciences*, *21*(1), 15-25. https://doi.org/10.1016/j.ejrs.2017.08.001

2. Akbari, H. (2000). Consideration of temperature distribution pattern of Tehran using Landsat TM thermal data. [MA dissertation, Tarbiat Modarres University]. https://ganj.irandoc.ac.ir. (In Persian).

3. Al-Hatab, M., Amany, S., & Lamia, T. (2018). Monitoring and assessment of urban heat islands over the Southern region of Cairo Governorate, Egypt. *The Egyptian Journal of Remote Sensing and Space Sciences*, *21*(3), 311-323. https://doi.org/10.1016/j.ejrs.2017.08.008

4. Chander, G., Markham, B., & Helder, D. (2009). Summary of current radiometric calibration coefficients for Landsat MSS, TM, ETM+, and EO-1 ALI sensors. *Remote Sensing of Environment*, *113*. https://doi.org/10.1016/j.rse.2009.01.007

5. El-Hadidy, Sh.M. (2021). The relationship between urban heat islands and geological hazards in Mokattam plateau, Cairo, Egypt. *The Egyptian Journal of Remote Sensing and Space Sciences*, *24*. https://doi.org/10.1016/j.ejrs.2021.02.004

6. Galdies, C., & Lau, H.S. (2020). Urban heat island effect, extreme temperatures and climate change: A case study of Hong Kong SAR. *Climate Change, Hazards and Adaptation Options*. https://link.springer.com/chapter/10.1007/978-3-030-37425-9_20

7. Guo, A., Yang, J., Xiao, X., Xia, J., Jin, C., & Li, X. (2019). Influences of urban spatial form on urban heat island effects at the community level in China. *Sustainable Cities and Society*, *53*. https://doi.org/10.1016/j.scs.2019.101972

8. Harun, Z., Reda, E., Abdulrazzaq, A., Amer Abbas, A., Yusup, Y., & Zaki Sh.A. (2020). Urban heat island in the modern tropical Kuala Lumpur: Comparative weight of the different parameters. *Alexandria Engineering Journal*, *59*. https://doi.org/10.1016/j.aej.2020.07.053

9. Kabano, P., Lindley, S., & Harris, A. (2020). Evidence of urban heat island impacts on the vegetation growing season length in a tropical city. *Landscape and Urban Planning*, *206*. https://doi.org/10.1016/j.landurbplan.2020.103989

10. Koopmans, S., Heusinkveld, B.G., & Steeneveld, G.J. (2020). A standardized physical equivalent temperature urban heat map at 1-m spatial resolution to facilitate climate stress tests in the Netherlands. *Building and Environment*, *181*. https://doi.org/10.1016/j.buildenv.2020.106984

11. Lemus-Canovas, M., Martin-Vide, J., Moreno-Garcia, M.C., & Lopez-Bustins, J.A. (2019). Estimating Barcelona's metropolitan daytime hot and cold poles using Landsat-8 Land Surface Temperature. *Science of the Total Environment*, *699*. https://doi.org/10.1016/j.scitotenv.2019.134307

12. Li, H., Zhou, Y., Jia, G., Zhao, K., & Dong, J. (2021). Quantifying the response of surface urban heat island to urbanization using the annual temperature cycle model. *Geoscience Frontiers*, *13*. https://doi.org/10.1016/j.gsf.2021.101141

13. Lia, L., Zha, Y., & Zhang, J. (2020). Spatially non-stationary effect of underlying driving factors on surface urban heat islands in global major cities. *International Journal of Applied Earth Observation and Geoinformation*, *90*. https://doi.org/10.1016/j.jag.2020.102131

14. Liu, Ch., Yang, M., Hou, Y., Zhao, Y., & Xue, X. (2021). Spatiotemporal evolution of island ecological quality under different urban densities: A comparative analysis of Xiamen and Kinmen Islands, Southeast China. *Ecological Indicators*, *124*. https://doi.org/10.1016/j.ecolind.2021.107438

15. Makhdoom, M., Darwish Sefat, A., Jafarzadeh, H., & Makhdoom, A. (2004). *Environmental assessment and planning with geographic information systems "GIS"*. University of Tehran, Publishing and Printing Institute. https://www.gisoom.com/book/1826711/. (In Persian).

16. Macintyre, H.L., Heaviside, C., Cai, X., & Phalkey, R. (2021). The winter urban heat island: Impacts on cold-related mortality in a highly urbanized European region for present and future climate. *Environment International*, *154*. https://doi.org/10.1016/j.envint.2021.106530

17. Mendez-Astudillo, J., Lau, L., Tang, Y., & Moore, T. (2020). A new Global Navigation Satellite System (GNSS) based method for urban heat island intensity monitoring. *International Journal of Applied Earth Observations and Geoinformation*, *94*. https://doi.org/10.1016/j.jag.2020.102222

18. Portela, C.I., Massi, K.G., Rodrigues, T., & Alcântara, E. (2020). Impact of urban and industrial features on land surface temperature: Evidences from satellite thermal indices. *Sustainable Cities and Society*, *56*. https://doi.org/10.1016/j.scs.2020.102100

19. Rajeshwari, A., & Mani, N.D. (2014). Estimation of land surface temperature of Dindigul district using Landsat 8 data. *International Journal of Research in Engineering and Technology*, *3*. https://ijret.org/volumes/2014v03/i05/IJRET20140305025.pdf

20. Sadeghinia, A., Alijani, B., Ziaeian, P., & Khaledi, S. (2013). Application of spatial autocorrelation techniques in the analysis of the thermal island of Tehran. *Applied Research in Geographical Sciences*, *30*. https://www.sid.ir/en/Journal/ViewPaper.aspx?ID=354812. (In Persian).

21. Sekertekin, A., & Zadbagher, E. (2021). Simulation of future land surface temperature distribution and evaluating surface urban heat island based on impervious surface area. *Ecological Indicators*, *122*. https://doi.org/10.1016/j.ecolind.2020.107230

22. Tepanosyan, G., Muradyan, V., Hovsepyan, A., Pinigin, G., Medvedev, A., & Shushanik Asmaryan, Sh. (2020). Studying spatial-temporal changes and relationship of land cover and surface urban heat island derived through remote sensing in Yerevan. *Armenia Building and Environment*, *187*. https://doi.org/10.1016/j.buildenv.2020.107390

23. United Nations Department of Economic and Social Affairs. (2019). *World Urbanization Prospects: The 2018 Revision*, ISBN (PDF): 9789210043144. https://doi.org/10.18356/b9e995fe-en

24. VAN DE GRIEND, A.A., & OWE, M. (1993). On the relationship between thermal emissivity and the normalized difference vegetation index for natural surfaces. *International Journal of Remote Sensing*, *14*, 1119-1131. https://doi.org/10.1080/01431169308904400

25. Vasenev, V., Varentsova, M., Konstantinov, P., Romzaykina, O., Kanareykina, I., Dvornikov, V., & Manukyana, Y. (2021). Projecting urban heat island effect on the spatial-temporal variation of microbial respiration in urban soils of Moscow megalopolis. *Science of the Total Environment*, *786*. https://doi.org/10.1016/j.scitotenv.2021.147457

26. Wang, Y., Yi, G., Zhou, X., Zhang, T., Bie, X., Li, J., & Ji, B. (2021). Spatial distribution and influencing factors on urban land surface temperature of twelve megacities in China from 2000 to 2017. *Ecological Indicators*, *125*. https://doi.org/10.1016/j.ecolind.2021.107533